Hydrology and Earth System Sciences Discussions

Estimation of forest structure metrics relevant to hydrologic modeling using coordinate transformation of airborne laser scanning data

A. Varhola[1], G. W. Frazer[2], P. Teti[3], and N. C. Coops[1]

[1]Department of Forest Resources Management, University of British Columbia, 2231–2424 Main Mall, Vancouver, BC, V6T 1Z4, Canada
[2]Department of Geography, University of Victoria, 3800 Finnerty Road, Victoria, BC, V8P 5C2, Canada
[3]BC Ministry of Forests, Lands, and Natural Resource Operations, 200-640 Borland Street, Williams Lake, BC, V2G 4T1, Canada

Title Page

Abstract | Introduction

Conclusions | References

Tables | Figures

◄ | ►

◄ | ►

Back | Close

Full Screen / Esc

Printer-friendly Version

Interactive Discussion

Abstract

Accurate characterizations of the complex and heterogeneous forest architecture are necessary to parameterize physically-based hydrologic models that simulate precipitation interception, energy fluxes and water dynamics. While hemispherical photography has become a popular method to obtain a number of forest canopy structure metrics relevant to these processes, image acquisition is field-intensive and therefore difficult to apply across the landscape. In contrast, airborne laser scanning (ALS) is a remote sensing technique increasingly used to acquire detailed information on the spatial structure of forest canopies over large, continuous areas. This study presents a novel methodology to calibrate ALS data with in-situ optical hemispherical camera images to obtain traditional forest structure and solar radiation metrics. The approach minimizes geometrical differences between these two techniques by transforming the Cartesian coordinates of ALS data to generate synthetic images with a polar projection directly comparable to optical photography. We demonstrate how these new coordinate-transformed ALS metrics, along with additional standard ALS variables, can be used as predictors in multiple linear regression to estimate forest structure and solar radiation indices at any individual location within the extent of an ALS transect. This approach is expected to substantially reduce fieldwork costs, broaden sampling design possibilities, and improve the spatial representation of forest structure metrics directly relevant to parameterize hydrologic models.

1 Introduction

Forested environments create unique microclimatic conditions that modulate a wide array of biophysical processes tightly linked to components of the hydrologic cycle. Structural and physiological characteristics of forests and their relationship to evapotranspiration, interception, soil moisture and energy fluxes have therefore been intensively studied to develop physically-based models capable of simulating water dynamics in

diverse hydroclimate regimes (e.g. Wigmosta et al., 1994; Pomeroy et al., 2007; Kuraś et al., 2012). In snow-dominated regions, forests generally reduce the amount of snow present on the ground prior to the onset of spring due to snowfall interception and sublimation in the canopies. The attenuation of solar radiation as it passes through forest

5   structural elements is also of particular importance because it controls the rate and timing of snow melt, and hence strongly determines flooding risk levels and seasonal water availability (Varhola et al., 2010a).

Modeling snow interception, radiation attenuation and other biophysical processes requires a detailed characterization of vegetation structure. While the capacity of

10   forests to intercept snow is primarily affected by snow density, stand architecture and branch flexibility (Parviainen and Pomeroy, 2000), spatiotemporal patterns of light transmission through the canopies are created by the interaction between local solar paths, the anisotropy of diffuse sky brightness, cloud cover and the three-dimensional distribution of all canopy elements (i.e. foliage, branches, boles and gap space) (Hardy

15   et al., 2004). Variations of these factors can create an unlimited array of micro-environments within a forest, each with a distinctive gap distribution that ultimately determines how much of the falling snow and incoming radiation actually reaches the ground (Essery et al., 2007; Hardy et al., 2004). Characterizing sub-canopy snow dynamics and radiation regimes within a specific spatial unit thus requires quantification

20   of this structural complexity into numerical parameters readily available as inputs for hydrologic models.

Three of the metrics most commonly used to describe forest structure and its relationship to hydrologic processes are leaf area index (LAI), gap fraction (GF) and sky-view factor (SVF). Although LAI has several definitions (Bréda, 2003), it is gener-

25   ally described as the ratio of one-half of the total leaf area per unit of ground surface area (Chen et al., 1997). Despite known difficulties with the accurate estimation of LAI, one of its versions also known as effective LAI or plant area index (PAI) has become a key input parameter in physically-based hydrologic models because it directly affects rain and snow interception, wind speed reduction, and radiation attenuation in forested

environments (Ellis et al., 2010). GF is the fraction of view that is unobstructed by canopy elements in any particular angular direction (Welles and Cohen, 1996), equivalent to the probability of a light beam passing through the forest to reach a point near the ground (Danson et al., 2007). SVF, used to model absorption of longwave radiation by snow (Wigmosta et al., 2002), is usually defined in hydrologic models as the fraction of celestial (sky) hemisphere visible from a point near the forest floor (Sicart et al., 2004) and is calculated as a cosine-weighted 180° integration of GF (Frazer et al., 1999).

Several methods have been developed to directly or indirectly estimate LAI, GF, and SVF in the field. One instrument frequently used is the LI-COR[®] LAI-2000 Plant Canopy Analyzer (LAI-2000), which can provide LAI and GF by simultaneously comparing incoming diffuse radiation above and below the canopy (Welles and Norman, 1991). Hemispherical photography (HP) is another popular alternative that uses skyward-looking images taken from beneath the forest to estimate various attributes of canopy structure and to model light penetration over long periods of time (i.e., growing season). Both the LAI-2000 and HP are based on a hemispherical projection geometry usually comprising a wide field of view (∼ 180° for HP and 148° for LAI-2000), which is fundamental to provide multi-angular estimates of GF and, in HP, to account for local solar paths and the angular variation in diffuse sky brightness. Advantages of HP over the LAI-2000 are that HP does not require above-canopy measurements of diffuse sky radiation to compute GFs and provides a permanent image of the forest that can be processed with software tools to automatically obtain a variety of structural and site-specific radiation parameters (e.g. Gap Light Analyzer (GLA), Frazer et al., 1999; or Hemiview, Rich et al., 1999). Although HP is not free of bias in the presence of heterogeneous lighting conditions and is subject to certain subjectivity when manually binarizing the images to separate canopy and sky pixels, it has been validated as a tool to accurately model radiation regimes beneath forest canopies, provided that a few basic local parameters are known (Coops et al., 2004). Hardy et al. (2004), for example, compared above- and below-canopy incoming global solar radiation measurements

from pyranometers with radiation transmission estimates obtained from HP, and concluded that both agreed well enough to be interchangeably used in snow models.

One disadvantage of HP, however, is that image acquisition and processing are time-consuming and therefore cannot be easily applied to vast, remote areas (Essery et al., 2007). Light Detection And Ranging (LiDAR), on the other hand, is a remote sensing technology capable of providing three-dimensional representations of canopy structure over large, continuous regions. LiDAR sensors actively emit laser pulses and record the distance between sensor and target, providing point cloud-type representations of the scanned objects. LiDAR systems are generally classified as either Terrestrial Laser Scanning (TLS) or Airborne Laser Scanning (ALS) according to its platform, or as discrete or full-waveform according to the type of digitization filter (Lim et al., 2003). Discrete ALS sensors mounted on helicopters or airplanes at low flying altitudes (500–1000 m) are currently the most widely used LiDAR systems in forestry (Lee et al., 2009) due to their extensive spatial coverage and sampling densities of one to several laser returns per m^2 (Wulder et al., 2008).

There is a significant body of literature investigating the application of ALS to predict traditional stand attributes such as tree density, diameter, height, timber volume, biomass and forest cover (e.g. Lim et al., 2003; Lovell et al., 2003; Næsset 2002; Wulder et al., 2008), while only a few articles have directly compared ALS metrics with HP-derived stand parameters. Solberg et al. (2006), for example, parameterized models to estimate LAI from discrete ALS by fitting simple ALS return penetration ratios to LAI data obtained from HP and LAI-2000 measurements, with the aim of detecting and mapping defoliation caused by an insect outbreak in Norway. They found a strong linear relationship between the log-transformed inverse of vertical GF obtained from repeated ALS acquisitions and LAI estimated in the field. To improve the relationships, follow-up studies re-applied similar methodologies varying image pre-processing procedures (Hanssen and Solberg, 2007) and testing different ranges of ALS plot radii, tree species and ALS return configurations (Solberg et al., 2009; Solberg, 2010). These and comparable articles published by Riaño et al. (2004), Morsdorf et al. (2006),

Title Page

Abstract | Introduction

Conclusions | References

Tables | Figures

◄ | ►

◄ | ►

Back | Close

Full Screen / Esc

Printer-friendly Version

Interactive Discussion

Jensen et al. (2008, 2011), and Korhonen et al. (2011), all rely on regression-based estimates of LAI or GF using simple vertical ALS return ratios obtained from cylindrical plots as predictors. The studies recognize and conclude that the different perspectives and projection geometries associated with HP (upward-looking, angular) versus ALS (downward-looking, near-vertical) sensors make it difficult to establish an exact match between the two techniques.

The objective of this article is to develop a methodology to obtain HP-equivalent forest canopy GF, LAI, SVF and solar radiation transmission metrics at any location within a discrete ALS cloud of points. Our approach transforms the Cartesian coordinates of the ALS point cloud into a polar coordinate system to produce synthetic, upward-looking hemispherical images suitable for processing with specialized software (GLA). Metrics obtained from these images are then calibrated directly with real optical HP counterparts collected within a network of ground-reference sites. This novel approach has the following advantages compared to previous studies that have attempted to link ALS and HP metrics: (1) it is based on the same geometrical projection and therefore minimizes calibration errors; (2) it takes advantage of the entire functionality of GLA or Hemiview, including the calculation of forest structure parameters and a variety of light indices for user-defined requirements; (3) it is less restricted to any particular spatial resolution associated with ALS cylinder size (Zhao and Popescu, 2009); (4) does not require direct radiation measurements for validation due to the proven ability of HP to predict radiation regimes (Hardy et al., 2004); (5) is based on a paired one-on-one comparison of hemispherical images rather than plot averages, allowing a more detailed exploration of the ideal physical representation of canopies by ALS; and, finally, (6) it only requires raw ALS data and HP without relying on manual ground measurements, complimentary spectral remote sensing tools or sophisticated tree-reconstruction or stem mapping techniques (e.g. Roberts et al., 2005).

2 Methods

2.1 Study area

The study took place in central British Columbia (BC), Canada, near the cities of Quesnel and Vanderhoof (Fig. 1). For a decade, this area has been affected by an outbreak of mountain pine beetle (MPB) (*Dendroctonus ponderosae*) that significantly changed the landscape by defoliating and killing large continuous forests of lodgepole pine (*Pinus contorta*), the dominant species. The Interior Plateau of BC is characterized by cold, dry winters with snow cover for up to seven months every year; snow melt constitutes a main source of water during spring and is also associated with annual peak streamflow (Bewley et al., 2010). Since the physical processes that govern snow accumulation and ablation are highly sensitive to changes in forest cover, the impacts of forest disturbance on hydrologic regimes has recently been under intensive research in BC (Bewley et al., 2010; Boon, 2009; Coops et al., 2009; Teti, 2008, 2009; Uunila et al., 2006; Varhola et al., 2010b).

Seven forested plots established by Teti (2008) provided the model calibration data for this study, and are described in detail on Table 1. The first four plots are located in the Baker Creek watershed, near Quesnel, while the last three are southwest of Vanderhoof. All are characterized by their low-gradient, relatively flat terrain and each consists of 36 sampling points separated by 10 m to create a squared 50 × 50 m grid, as shown on Fig. 1. The plots are representative of the main stand types and their relative predominance in the area at the time of their installation, namely: mature stands (height > 15 m) where most of the trees had been severely defoliated by MPB (BOD1, BOD3, VOD1 and VOD2); intermediate (height ∼ 10 m) stands affected by MPB but with their trees still holding dehydrated, red foliage (BRC2); and young healthy-looking stands (height ∼ 3 m) (BRC1). An additional plot was located in a dense stand resulting from post-fire regeneration (VYN), with high stem densities and 25 % mortality caused by within-stand competition and ice/snow-related breakage rather than MPB. More information about these plots and the methodology for capturing inventory metrics and

MPB defoliation are available on Teti (2008). Eleven additional plots of a different size and configuration, which included other stand types such as healthy spruce, were used to validate our methodology at the plot-level.

2.2 Data acquisition for modeling

Hemispherical photographs were taken within 1 m of each of the 36 sampling points during the summer of 2008 using a Nikon Coolpix 4500 digital camera with a Nikkor FC-E8 auxiliary fisheye lens (view angle = 183°) mounted 110 cm above the ground as specified by Teti (2008). Although it is recommended to capture HP during overcast skies to favour maximum contrast with the canopy elements (Frazer et al., 2001), these ideal conditions are rarely present in central BC. To prevent sunlight from directly hitting the lens, Teti (2008) used a small shading paddle which was later eliminated from the images by careful retouching. The sampling points were registered by a GPS with differential correction, resulting in a maximum estimated deviation of 1.5 m between each point and the actual corresponding camera position.

ALS data were acquired in February 2008 by Terra Remote Sensing (Sidney, BC) with a TRSI Mark II discrete return sensor mounted on a Bell 206 Jet Ranger helicopter at a flying altitude of ∼ 800 m above ground level. The sensor's wavelength was 1064 nm with a pulse repetition frequency of 50 kHz, maximum off-nadir scan angle of 15°, and a fixed beam divergence angle of 0.5 mrad. A 200 km × 400 m ALS transect was acquired over the ground plots in four separate sections, as shown on Fig. 1, with a resulting average foot-print size of 0.35 m and an average effective density of 4.8 returns m^{-2}. To estimate plot center elevations, a 5 m^2 ground-level digital elevation model (DEM) was created by applying the ground filter algorithm used in FUSION® software (McGaughey, 2010) to the ALS data as proposed by Kraus and Pfeifer (1998).

A suite of basic ALS metrics were obtained for each 50 × 50 m plot to explore the overall variability of forest structure and data configuration (Table 2). The total number of ALS points per plot was separated into sub-canopy (below 0.5 m) and canopy (above 0.5 m) classes. ALS point density was calculated by dividing the total number of laser

returns by plot area (2500 m^2), while ALS metadata provided mean absolute scan angle directly. Vertical GF was calculated for each plot as the ratio of sub-canopy returns (> 0.5 m) to total ALS returns. Maximum canopy height was approximated as the height above ground of the single highest ALS return within each plot, and the mean canopy

5 height proxy was the average height above ground of all canopy returns (different from mean tree height). In all cases, no distinction was made between first and other return types.

2.3 Synthetic ALS hemispherical image generation

ALS data was extracted for 75 m radius cylinders centered at each of the sampling

10 points, a size chosen to ensure that enough ALS returns were included closer to the horizon to mimic the infinite viewing distance of optical HP, yet small enough so that the entire cylinders fit in the 400 m-wide data transect. Only the three northernmost rows of plot VOD1 were excluded as they were too close to the ALS boundary, thus reducing the sample to a total of 234 cylinders. All the ALS returns (first, intermediate, last) were

15 included in the cylinders to maximize density as proposed by Todd et al. (2003) and Lee et al. (2009).

Each Cartesian (XYZ) reference position was set to 60 cm above the ALS DEM to account for the fact that ALS was collected during winter when ground returns recorded a snow layer averaging 50 cm of depth (Coops et al., 2009) rather than the bare soil

20 where the HP camera was later positioned. ALS returns at elevations below the camera's maximum field of view were eliminated from the 75 m cylinders to increase data processing efficiency. The XYZ positions of all the remaining returns were transformed with simple trigonometry to polar coordinates composed of angles of azimuth (°) and zenith (°), and distance (m) with respect to each HP reference position. Finally, angles

25 of azimuth were flipped in an east-west direction to reflect an upward-looking field of view as in HP.

The fine-scale representation of physical vegetation structure by individual ALS returns is not well understood, and several assumptions are therefore required to convert one-dimensional (1-D) laser points into geometrically simplified, 3-D plant structures. We undertook a sensitivity analysis on a subsample of calibration plots to explore the impact of three main parameter settings related to projected canopy element size and shape: (1) projecting returns with a fixed or variable size (inversely proportional to distance), or a combination of the two; (2) minimum ALS return circle size for fixed projections; and (3) ALS return sphere size for variable projections. More details about these parameters and their implications are clarified below as the methodology for generating the synthetic images is explained. The optimal parameter settings were chosen by evaluating scatter plots and correlation coefficients of observed GFs in real versus synthetic images, while keeping the other parameters constant. Figure 2 shows an example testing three different minimum fixed projected sizes.

Based on the results of the sensitivity analysis, each ALS return was represented as an opaque sphere with a 15 cm diameter centered on the original ALS XYZ point location. These spheres were projected as black circles on a two-dimensional plane to create one synthetic hemispherical image for each sampling cylinder. Calculating the diameter of the each projected ALS point first required the selection of an arbitrary radius for the circular images and a theoretical focal length, both 10 cm. The ratio between the projected and full-scale ALS return radii is then assumed equivalent to the ratio between the focal length and the absolute distance between the return's centroid and the camera position.

Optical distortions typical of hemispherical lenses were accounted for when generating the synthetic images. When viewed from a distance d, a sphere subtends an angle equal to the arctangent of the ratio between the sphere's diameter and d. A sphere located along the optical axis of a fisheye lens (i.e. at zenith $= 0°$ in this case) appears as a circle when projected on the image and gradually flattens into an ellipse as the azimuthal diameter is stretched in proportion to the zenith angle. This can be illustrated by considering the polar coordinate representation of three points in the celestial

LiDAR canopy metrics relevant to hydrological modeling

A. Varhola et al.

hemisphere – one at the zenith, one at the east horizon, and one at the north horizon. In polar coordinates, the line connecting the zenith with one of the points on the horizon has a length equal to the image radius (r) whereas the line connecting the two points on the horizon has a length of $\pi \times r/2$, even though the angular separation between all three points is 90°. Thus, the apparent area of a feature in a hemispherical image increases from zenith to horizon according to $Z/90 \times \pi/2$, where Z (°) is the zenith angle of the feature (e.g. a sphere projected in the horizon (90°) appears with its azimuthal radii $\pi/2$ (57 %) larger than a sphere at the zenith). To simplify plotting synthetic images, we used circles to represent the modeled ALS returns with their areas increased to account for the stretching.

The radial location of ALS returns in the synthetic images followed the same equiangular projection produced by the optical lens system (FC-E8 fisheye converter) used to collect the real HP images (Inoue et al., 2004), where the radial distance from the center of the image is directly proportional to the zenith angle (Rich et al., 1999). A projection based solely on variable diameters resulted in unrealistic-looking images with distant points appearing too small to be detected as dark pixels. To avoid this, a minimum base constant return diameter (2.15 mm within a 20 cm diameter image, in this case; Fig. 2) was assigned to all returns in the images so that only those points close enough to the HP reference to exceed this diameter were projected at variable, larger sizes. Finally, ALS returns closer than 75 cm to the reference were eliminated in accordance with the HP field procedures, which specified a minimum distance between foliage and camera lens for protection purposes and to eliminate the possibility of having a large proportion of the optical field of view obscured by a single foliage unit.

Each synthetic image was generated as a 750×750 pixel bitmap image file (BMP). All 234 files were automatically created in 5 min and 15 s using MATLAB® ($1.3\,\text{s image}^{-1}$) on a 2.66 GHz, 4.0 GB RAM, 64-bit computer.

2.4 Data processing

2.4.1 HP analysis

Both optical HP and ALS synthetic images were analyzed with GLA using the parameters listed on Table 3. The binarization thresholds required for optical HP were provided by Teti (2008), while synthetic ALS photos were logically generated in black and white. GLA processing was done manually for each of the 468 images (optical and synthetic) at a rate of around 17 s per file (excluding HP binarization). Table 4 describes the output variables obtained from the GLA analysis for each HP and synthetic image for the 234 sample locations. All of the variables except LAI were numerically integrated across the following zenith angle of view (AOV) (θ): 0–30, 0–45, 0–60, 0–75 and 0–90°. Lower zenith angle limits were included here to allow later explorations of their relationships with hydrologic processes, based on previous findings. Teti (2003), for example, concluded that a 0–30° zenith AOV was most effective at explaining differences in snow storage in the presence of different sized gaps. In addition, sky regions including the 0–45° and 0–60° zenith ranges contain most of the solar paths directly responsible for spring melt in our study area. $FLAI_{\theta}$ and $LLAI_{\theta}$ (defined on Table 4) automatically integrate LAI for zenith angles of 60 and 75° (Welles and Norman, 1991; Stenberg et al., 1994).

In light of intensive theoretical discussions and controversies about true LAI derivation for decades (Bréda, 2003), we highlight that this study is only focused on the version of LAI that has been widely used in hydrologic models: that obtained from LAI-2000 or HP, commonly known as effective LAI (LAI_e) or plant area index (PAI) (e.g. Pomeroy and Dion, 1996; Bewley et al., 2010). It is not our goal to correct for clumping, isolate foliage from stems or formulate hypotheses about the angular distribution of leaves because more nuanced (or simply different) versions of LAI would also require the reparameterization of existing hydrologic models. In this respect, LAI obtained from optical HP is considered as our ground-truth variable.

Title Page

Abstract | Introduction

Conclusions | References

Tables | Figures

◄ | ►

◄ | ►

Back | Close

Full Screen / Esc

Printer-friendly Version

Interactive Discussion

2.4.2 Standard ALS metrics

The traditional ALS metrics (without coordinate transformation) listed in the bottom of Table 4 were calculated from variable-size cylinders whose diameter hypothetically intercepted the canopies at each zenith AOV (θ) based on plot-level maximum tree height (Table 1) (for $\theta = 90°$, cylinder diameters calculated for $\theta = 75°$ were used). From these point clouds, vertically projected gap fraction (LVGF), mean laser canopy height (LMH), return density (LD) and scan angles (LSA) were estimated for each of the field plot locations (Table 2). LVGF and LMH are important descriptors of stand structure, while LD and LSA are related to ALS sensor configuration and data acquisition conditions, all potentially important sources of variation as shown in Table 2. More specifically:

– LVGF represents a downward-looking ALS ground-to-canopy return penetration ratio known to be well correlated with upward-looking HP sky/canopy GFs (Solberg, 2010).

– LMH is an indicator of stand height and provides substantial differentiation between stands.

– LD accounts for the varying ALS return density among plots (see Table 2) produced by changing flight altitude and speed (Bater et al., 2011; Goodwin et al., 2006), which can alter the probability of ALS returns being intercepted by the canopy. Varying patterns of flight line overlap may also contribute to markedly different laser point densities throughout the spatial coverage, and must be explicitly accounted for when neighboring or intersecting datasets result in higher numbers of returns (our ALS data was restricted to a single flight line and not subject to changes in density due to overlap).

– LSA increases from the centre of the flight line (nadir) towards the swath edge and changes the probabilities of ALS hitting different canopy sections. For example, if scan angles are too large, laser pulses are less likely to penetrate the canopy

Title Page

Abstract | Introduction

Conclusions | References

Tables | Figures

◄ | ►

◄ | ►

Back | Close

Full Screen / Esc

Printer-friendly Version

Interactive Discussion

Discussion Paper | Discussion Paper | Discussion Paper | Discussion Paper

because of the longer path length, resulting in a different spatial representation of the forest (Korhonen et al., 2011).

2.5 Regression modeling

GF, LAI, SVF and total direct and diffuse (global) radiation transmittance are GLA outputs directly applicable in hydrologic simulators (e.g. Wigmosta et al., 1994), and were therefore selected as the main response variables in this study (Table 4). To simplify the regression analyses, given the large number of variables and zenith AOV combinations, a specific modeling strategy was designed to ensure that all models: (1) shared a unique, stable structure; (2) were applicable to the full range of sampling points, avoiding the need to pre-identify different forest populations or use indicator (dummy) variables; and (3) were intrinsically linear (avoiding predictor variable transformations or nonlinear regression techniques).

Both simple and multiple linear regression analyses were applied to predict the four HP-derived metrics:

$$Y_{S(\theta)} = b_0 + b_1 X_{1(\theta)} \tag{1}$$

$$Y_{M(\theta)} = \beta_0 + \beta_1 X_{1(\theta)} + \beta_2 X_2 + \beta_3 X_3 + \beta_4 X_4 + \beta_5 X_5 \tag{2}$$

where θ is the maximum zenith AOV for metric aggregation (30, 45, 60, 75 and 90°); Y_S and Y_M can be either FGF_θ, FRT_θ, $FSVF_\theta$ or $FLAI_\theta$; X_1 is the ALS-derived counterpart of Y_S or Y_M (LGF_θ, LRT_θ, $LSVF_\theta$, or $LLAI_\theta$, respectively); X_2 corresponds to LVGF, X_3 is LMH; X_4 is LD; and X_5 is LSA. Please refer to Table 4 for a comprehensive definition of these variables.

Correlations between the dependent variables and each of the independent variables were examined through scatterplots, and a correlation matrix between all predictor variables (plus FGF_θ) was produced to ensure that variables with high inter-correlations were not added to the models.

Equations (1) and (2) were fit using ordinary least-squares regression for each zenith AOV (θ) metric. Also, in order to justify the need and benefit of performing ALS

Title Page

Abstract | Introduction

Conclusions | References

Tables | Figures

◄ | ►

◄ | ►

Back | Close

Full Screen / Esc

Printer-friendly Version

Interactive Discussion

coordinate transformations, a simple linear model was fit to predict HP gap fraction (FGF$_\theta$) with the vertical ALS gap fraction (LVGF) only ($Y_{S(\theta)} = \beta_0 + \beta_2 X_{2(\theta)}$).

Goodness of fit was evaluated based on the models' adjusted coefficients of determination (r^2 and R^2) and three versions of root mean squared error: absolute (RMSE),
split-sampling average derived by iteratively refitting the model with all but 1 of 9 randomly generated data groups (RMSE$_S$), and normalized by the range of observed values to enable comparisons between different variables (RMSE$_N$). All models were validated by observing the significance probability (p) of the regression coefficients and by performing Anderson-Darling and Shapiro-Wilk normality tests on the residuals, which
confirm the required normality if $p > \alpha$ (in all tests, $\alpha = 0.05$). Linearity and variance stability was assessed through visual inspection of predicted vs. observed and predicted vs. residual scatterplots. 95 % prediction and confidence intervals were calculated and illustrated on the predicted vs. observed figures. For multiple regression, the confidence intervals were estimated with a quadratic function relating individual predicted values
to their corresponding lower and upper limits as generated by the statistical software ($I = c_0 + c_1 \times P + c_2 \times P^2$, where I = upper or lower interval limit, P = predicted value and c_0, c_1 and c_2 are model coefficients). Variance inflation factors were also estimated to check for multicollinearity (Field, 2005).

Choosing the best common multiple regression model structure followed a manual
backward stepwise approach for variable selection. The intercept and all five predictor variables (Eq. 2) were initially included in the regression to obtain a matrix of coefficient p values that included the entire response variable – zenith AOV model combinations. Model coefficients of the supporting predictor variables ($X_2 \ldots X_5$) that were not significant more than twice in the matrix were removed until only those variables consistently
showing statistical significance across all models were identified. The equations were then validated using the tests described above.

Title Page

Abstract | Introduction

Conclusions | References

Tables | Figures

◄◄ | ►►

◄ | ►

Back | Close

Full Screen / Esc

Printer-friendly Version

Interactive Discussion

2.6 Plot-level ground-truth model validation

Using the methodologies presented here, new and different grids of synthetic hemispherical images were generated in the same calibration plots and an additional set of 11 plots (other than those in Table 1) as part of a follow-up study. The resulting average GFs were compared with those estimated from pre-existing optical HP available in these plots. Although the number and distribution of synthetic and optical HP differed substantially within each plot, this comparison was very useful to validate our methodology with an independent dataset and justify the need of ALS coordinate transformation even if plot-level averages are required. This was done by contrasting the relationship between optical HP-derived GFs and both a simple ratio of raw ALS ground/canopy returns and GFs derived from synthetic hemispherical images.

3 Results

3.1 Preliminary sensitivity analysis

The sensitivity analysis applied to a sub-sample of images indicated that the projection of ALS spheres using inverse distance-weighted diameters generally had little effects for the majority of synthetic images generated in mature stands, due to the large distances between the returns and the projection reference. Increasing the theoretical diameter of the spheres beyond 15 cm only made returns close to the reference appear too big and block significant portions of the image, while substantially deteriorating the relationship between synthetic and optical estimates of GFs. However, variable-diameter projections were still necessary to produce an adequate representation of canopy structure in the young regeneration stand, where 15 cm spheres appeared optimal in all cases. On the other hand, varying the minimum size of projected returns affected the slope of the calibration relationships (hence altering r^2) but did not show a discernible scatter reduction (Fig. 2).

Title Page

Abstract | Introduction

Conclusions | References

Tables | Figures

◀ | ▶

◀ | ▶

Back | Close

Full Screen / Esc

Printer-friendly Version

Interactive Discussion

3.2 ALS-derived synthetic hemispherical photos

Figure 3 shows examples of ALS point clouds with corresponding synthetic and actual HP for six common stand structure types found in the study site. In general, there is good visual agreement between the HP and synthetic images across the stands, although the point density (5–8 points m^{-2}) of this ALS dataset makes identification of individual trees difficult. In the taller stands (BOD1-C5, BOD3-C4), larger and continuous gaps in the forest canopy are apparent at smaller zenith angles of both the actual and synthetic images. Denser and more homogeneous canopies (BRC2-C1, VYN-B4) show a more even distribution of canopy elements (i.e. ALS returns) across all the zenith angles. Markedly different to the other stands is the young regeneration (BRC1-A3), where images are dominated by sky and shorter, clumped vegetation leads to interception of ALS returns much closer to the projection reference.

3.3 Relationships between variables

The correlation matrix between GF as derived from the actual HP (FGF$_\theta$) and estimated from the synthetic images (LGF$_\theta$) for the five zenith AOV is shown in Table 5. The relationship between the ALS and HP-derived GFs is significant at all zenith angles and becomes stronger as zenith AOV increases ($r = 0.75$ for $\theta = 30°$ and $r = 0.93$ for $\theta = 90°$).

In addition, Table 5 summarizes correlations between the two angular GFs (FGF$_\theta$ and LGF$_\theta$) and the ALS simple metrics (LVGF, LMH, LD, LSA), which are generally poor. The best correlation occurred between mean LMH and LGF$_\theta$, suggesting that taller stands have a smaller GF across all zenith angles. The correlations between the predictor variables to be input in the multiple regression model (Eq. 2) are generally weak, so redundancy is not likely introduced.

Scatterplots between FGF$_\theta$ and LGF$_\theta$ are shown for all zenith AOV on Fig. 4a–c. Differences in structure across the stands result in distinct population clusters clearly visible in the figures, which prevent fitting a single model to the data.

The relationship between LGF_θ and FGF_θ shows that, with the current parameter setup, the synthetic images underestimate GF when compared to HP, with the exception of stand BOD3. The young regeneration stand (BRC1) also deviates from the LGF_θ–FGF_θ general linear pattern and shows a considerably higher variability.

3.4 Simple linear regression

A simple regression model predicting FGF_θ from ALS untransformed data (LVGF) was weak across all zenith AOV (r^2 ranging from 0.31 to 0.41). Adjusted r^2 values increased (0.59–0.87) and RMSE decreased when the ALS transformed variable (LGF_θ) was used; however, nearly all the simple linear regression models failed residual normality tests. This is illustrated in Fig. 4d–f, where scatterplots of observed vs. predicted gap fractions indicate that a single regression line does not account for different populations of stand structures, particularly within the short regeneration stand (BRC1).

3.5 Multiple linear regression

After applying multiple regression to Eq. (2) with all the predictor variables included, LMH proved to be non-significant for θ values of 30° and 45° in all cases and for $FLAI_{60}$ and $FLAI_{75}$, while LSA was consistently non-significant across all model specifications. The intercept (β_0) and LVGF were not significant in two cases only and were therefore not excluded for a second run. After eliminating LMH and LSA from the regression, all of the remaining parameters were statistically significant with no exception. However, models for $\theta = 30°$ did not pass the two residual normality tests, and the $FLAI_{60}$ model barely passed the Anderson-Darling test only. As suggested by Kutner et al. (2005), transformations of the response variable Y_M were attempted to solve non-normality of residuals in these cases while maintaining our modeling strategy. None of the transformations tested (i.e. inverse, square, square-root, log) solved the problem for FGF_{30}, FRT_{30}, and $FSVF_{30}$. However, replacing $FLAI_\theta$ with $FLAI_\theta^{0.5}$ allowed the models to pass

Title Page

Abstract | Introduction

Conclusions | References

Tables | Figures

◄ | ►

◄ | ►

Back | Close

Full Screen / Esc

Printer-friendly Version

Interactive Discussion

the Anderson-Darling test without losing variable significance while improving R^2 and RMSE.

Thus, the model that complied with the all the conditions was:

$$Y_{M(\theta)} = \beta_0 + \beta_1 \times X_{1(\theta)} + \beta_2 \times X_2 + \beta_4 \times X_4 \qquad (3)$$

Regression results for Eq. (3) are provided in Table 6, which show that model behaviour was very similar for all dependent variables. Adjusted R^2 improves as zenith AOV increases due to more pixel aggregation that reduces the probability of canopy returns being assigned to the wrong sky region. $RMSE_N$ are very similar for FGF_θ, $FSVF_\theta$ and FRT_θ with the same θ, while the prediction accuracy of all models is validated by the consistent similarities between RMSE and $RMSE_S$ (Kutner et al., 2005). The fitted parameter estimates of β_0, β_1, β_2 and β_4 shown in Table 6 can be readily used to predict FGF, FSVF, FRT and FLAI at location within the current ALS data. All models produced variance inflation factors ranging between 1.3 and 1.7, eliminating multicollinearity concerns (Myers, 1990).

Scatterplots of predicted vs. observed values of FGF_θ are shown in Fig. 4g–i for $\theta = 30$, 60 and 90°, respectively. When comparing Fig. 4d–f to Fig. 4g–i, it is evident that multiple linear regression was a successful tool to achieve more accurate predictions, especially by accounting for the distinct stand structure of the young regeneration stand (BRC1). Figure 4d, g also show that outliers might be preventing model validations for $\theta = 30$°. Scatterplots of predicted GFs and the model residuals appear visually satisfactory for all zenith AOV (Fig. 5).

Figure 6b indicates that plot-level GF averages from optical HP are closely related to averages from new synthetic ALS images, both obtained for all the plots where ALS was available in the study area. The comparison between Fig. 6a, b constitutes strong evidence to justify coordinate transformation to accurately predict GF.

Title Page

Abstract | Introduction

Conclusions | References

Tables | Figures

|◄ | ►|

◄ | ►

Back | Close

Full Screen / Esc

Printer-friendly Version

Interactive Discussion

4 Discussion

The discussion regarding the methodology presented in this study is centered around the following questions: (1) how do synthetic hemispherical ALS images visually compare to their real HP counterparts and what are the main sources of error?; (2) how
5   suitable is discrete ALS to represent the fine-scale canopy elements responsible for radiation transmission?; (3) how effective was the proposed modeling strategy?; (4) what are the perceived benefits of the methodology?; and (5) what lines of action are needed to improve and apply this approach in future research?

4.1 ALS synthetic hemispherical images

10   Our results indicate that coordinate transformation of ALS data produced synthetic HP images which were qualitatively and quantitatively similar to real optical HP. The use of a 75 m diameter ALS cylinder was deemed appropriate for this dataset, given that enough spheres appeared in the synthetic images at higher zenith angles to reproduce the saturation that occurs in real HP under closed canopy conditions. If needed, smaller
15   cylinders could be tested for narrower ALS transects. We expect that any correction for the increasing geometrical distortion of projected spheres at larger zenith angles would have little impact on the results, largely because of the increased overlap and saturation that also occurs at these same view angles. A visual inspection of the synthetic HP dataset showed that individual trees were difficult to identify in most stands, and that
20   ALS returns occasionally appeared where canopy elements were absent in HP. There are three possible explanations for these differences: (1) density of the ALS point cloud was too low to capture basic crown-level structural details apparent in the optical HP; (2) HP was acquired six months after ALS and changes in stand structure (e.g. crown damage, tree fall, etc.) could have occurred in these stands affected by MPB, and (3)
25   there were GPS positional errors in HP plot locations, as well as camera orientation and image registration errors.

4.2 Physical representation of canopy elements with ALS

Successful transformation of the ALS point cloud into realistic synthetic HP images depends on a number of factors. First, the density of laser points needs to sufficient enough to capture the basic geometry of individual tree crowns and branches. Second, the size and shape of projected synthetic canopy elements (in this case spheres) must be closely related to some basic unit of light-intercepting foliage or branch structure found in real forests. Third, the density and distribution of laser points must be relatively uniform throughout the entire survey area to avoid bias.

It was shown here that a minimum constant projected size was necessary for all returns to resemble HP; however, inverse-distance-weighted variable projections were still necessary for returns closer to the reference, particularly for the short regeneration stand. ALS returns portrayed as opaque spheres represent a crude approximation of canopy structure as seen by a camera. Real canopy elements are far more complex, but because it is impossible for discrete ALS returns to accurately characterize fine-scale details of plant canopies, some arbitrariness is inevitable when assigning theoretical shapes and sizes to ALS returns. It must be highlighted that our methodology was not designed to reproduce the scale of detail found in real HP images as possible with higher density TLS (Côté et al., 2009), but to capture the basic patterns of canopy structure responsible for light interception and penetration that may in turn influence snow accumulation and melt.

The detection of canopy elements by ALS and a HP are both dependent on optical properties of the canopy; however, the former technique is based on reflectivity while the latter on opacity. Another disparity between HP and ALS is that the downward, near-nadir view angle of ALS provides a biased vertical profile of forest canopies in which upper elements have a higher probability of being detected, leading to an underrepresentation of lower branches and stems (Hilker et al., 2008). This may be compensated in synthetic ALS hemispherical projections because image saturation increases towards the horizon mainly due to the corresponding exponential increase in

Discussion Paper | Discussion Paper | Discussion Paper | Discussion Paper | Discussion Paper

the number of ALS returns, while in HP it is common to observe tree stems closer to the camera occluding the farther views as the main source of saturation. This will have an effect on the amount of unexplained variance in the regression models, but the strength of model fits (adj. R^2 = 0.8 to 0.92) for FGF, FSVF, FRT, and FLAI suggest that any bias in height distribution has little effect on the results. Any shortcoming is unavoidable in the absence of more sophisticated individual tree-reconstruction routines, but the corresponding uncertainties here are partly masked and absorbed by the calibration models.

In this study, we made several assumptions about the size and shape of a specific combination of predictors and parameter estimates were chosen so that the empirical relationship between canopy metrics derived from synthetic and real HP and their visual similarity was maximized. This methodology, empirical in nature, is admittedly susceptible to interactions between parameters. For instance, a larger base fixed projected circle size might be needed if ALS return density is lower, or the maximum sphere size could be reduced if returns are too close to the reference. Applying this methodology to a wider combination of forest stands and ALS datasets is required to evaluate parameter stability and optimization.

4.3 Modeling strategy

Regression models using simple vertical gap fraction (LVGF) to estimate HP metrics generally had low r^2, high $RMSE_N$ and produced model residuals that failed normality tests. These results contrast with those of Solberg et al. (2006, 2009), Hanssen and Solberg (2007) and others, in part because their statistical comparisons were based on the average of multiple photo plots rather than individual photo points, masking within-plot variability. Simple linear regression directly estimating HP metrics from their ALS-derived counterparts (X_1) was also unsuccessful because it failed to include other key explanatory variables (namely LVGF and LD) describing the relationships among all stands in one single model, especially due to the deviations shown by BRC1 and BOD3

(Fig. 4). However, the need to perform coordinate transformations of ALS data to better predict HP-derived metrics in individual sampling points was strongly justified (Fig. 6).

Multiple linear regression was an appropriate tool to calibrate ALS metrics with HP by accounting for both forest structure and data configuration properties. The models' R^2 values above 0.80 and $RMSE_N$ below 10 % across all zenith AOV higher than 45° suggest that confident predictions can be made throughout the entire ALS transect. This idea is also supported by the wide structural diversity of stands included in the regression dataset and the successful validation performed at plot-level averages in additional stands which represented even more diverse conditions (Fig. 6). Better HP geographical registrations and simultaneous HP/ALS data collection plus a detailed outlier analysis are required to fully validate the models for $\theta = 30°$.

A strong component of this study involved the use of a large network of individual ground-reference samples representing a heterogeneous collection of forest structure conditions that appropriately represented both within- and between-stand variability. The latter was particularly important to understand the relationship between GF derived from ALS synthetic images and HP across a broad range of GF estimates (e.g. 0.3 to 0.9 for $\theta = 60°$, Fig. 4h). A more complete sample of stand structures would have included mature, non-defoliated pine stands; however, this stand type was absent from the study area at the time of data collection. The accuracy of predicting HP metrics directly with ALS synthetic counterparts, however, should be independent of stand health status in light of both ALS and HP being able to detect defoliation (Solberg et al., 2006).

The developed models (Eq. 3, Table 6) proved suitable for our range of sampled forest structures and ALS data. Consequently, they need to be tested and validated for different stand types (species, densities, heights, health, etc.) and other ALS data acquisitions (e.g. point density, scan angle, footprint size, overlapping transects, return classes, etc.). Despite the supporting ALS vertical variables increasing the significance of the model if applied to alternative datasets, new HP/ALS calibrations are required every time this approach is applied in a different area. This includes reassessing variable significance and full model validation. It is especially important to account for changes

in ALS density caused by systematic overlapping multiple transects, where duplicate sampling might not be properly captured by LD alone. A voxelization of the ALS point cloud could minimize the effect of varying point densities, whereby each volume element (voxel) is coded as one if occupied by one or more ALS returns, or as zero if
5 empty (Côté et al., 2009).

4.4 Methodological advantages and applicability

There are a number of advantages associated with transforming ALS coordinates to generate hemispherical synthetic images. First, geometrical discrepancies between ALS and HP are minimized, allowing a direct comparison of structural and radiation
10 metrics at the individual point level. Second, the methodology is simple because it is based on raw ALS point-cloud data and avoids the need for elaborate canopy models, separation of ALS points into ground and non-ground classes, and voxelization. Third, GLA or other specialized programs can be used to directly estimate GF, LAI, SVF and local transmission of direct, diffuse or total radiation through forest canopies.
15 Fourth, as opposed to previous studies linking HP or LAI-2000 metrics with ALS plots of a specific diameter that restricts the spatial resolution of the analyses, generating synthetic hemispherical images from ALS introduces unlimited flexibility in terms of sample size and experimental design layouts: any number images can be obtained at user-defined spacing options and sub-pixel specific locations. Finally, variables directly
20 applicable to hydrologic modeling can now be obtained at any point within ALS datasets – significantly reducing fieldwork requirements while improving the parameterization of vegetation classes at the landscape-level.

4.5 Future work

Further research should focus on (1) improving the accuracy of the methodology by
25 better geographical registration methods and coordinated data collection; (2) validating or reformulating the current models using different datasets and study areas (e.g.

Title Page

Abstract | Introduction

Conclusions | References

Tables | Figures

|◄ | ►|

◄ | ►

Back | Close

Full Screen / Esc

Printer-friendly Version

Interactive Discussion

other species, mountainous topography) to evaluate parameter stability; (3) explore the relationships between structural variables obtained from synthetic ALS hemispherical images and satellite-derived spectral indices for watershed- or landscape-level extrapolations; and (4) improve the functionality of HP processing algorithms to estimate radiation components at sub-daily time steps (e.g. Leach and Moore, 2010). The latter represents a difficult challenge given the inaccuracies in camera orientation, anisotropy of sky brightness and atmospheric attenuation, among others; however, if achieved, would allow the direct input of radiation transmission into point-based process simulation of hydrologic models and better performances if above-canopy radiation is available.

While GLA can directly estimate GF and radiation transmission, most hydrologic models have used LAI as the forest structure parameter input to calculate hourly or daily radiation components (e.g. Wigmosta et al., 1994; Pomeroy et al., 2007). Nevertheless, the difficulties to accurately measure true LAI in the field are well known, and optical methods only measure the effective plant area index unless corrections are made for foliage clumping and the surface area contributed by branches and boles (Bréda, 2003). LAI-2000 or HP processed with GLA are also impacted by this bias and yet remain a popular method to estimate LAI by integrating log-transformed gap fractions through cosine-weighted zenith rings (Welles and Norman, 1991), only to be used as an intermediate parameter to simulate radiation transmission and other processes in hydrologic models. However, since radiation transmission and all the light indices available from GLA are also directly obtained from the simple sky/canopy pixel ratio defined here as gap fraction (GF), this variable might constitute a conceptually simpler and more parsimonious average forest structure parameter than LAI when modeling below-canopy radiation regimes. New studies are required for re-parameterizing hydrologic models to substitute LAI with GF, and to quantify the resulting benefits/losses.

5 Conclusions

To our knowledge, this is the first study that has attempted to re-project discrete ALS individual returns in a polar coordinate system to directly model forest structure and radiation regimes with currently available HP image processing tools. Our results suggest that reprojection of the ALS point cloud is necessary if accurate estimates of canopy gap fraction and solar radiation transmission are required at the point level.

It was not the goal of this study to provide prediction models with universal application across all forest types and ALS datasets, but to reveal the importance of coordinate transformation for the estimation of GF and other bulk-canopy metrics, and to demonstrate that these variables can be predicted from discrete ALS calibrated with HP. Our main research objective was fulfilled with the current approach as the models developed can operationally predict canopy GF, LAI, SVF and light indices with reasonable accuracy in any location within this ALS dataset, regardless of forest type. As ALS is becoming increasingly available worldwide, this article represents a major contribution to hydrologic studies by facilitating the estimation of forest structure metrics relevant to model parameterization through reduced fieldwork requirements and unlimited, spatially-explicit sampling designs.

References

Bater, C. W., Wulder, M., Coops, N. C., Nelson, R. F., Hilker, T., and Næsset, E.: Stability of sample-based scanning-LiDAR-derived vegetation metrics for forest monitoring, IEEE T. Geosci. Remote, 49, 2385–239, 2011.

5 Bewley, D., Alila, Y., and Varhola, A.: Variability of snow water equivalent and snow energetics across a large catchment subject to Mountain Pine Beetle infestation and rapid salvage logging, J. Hydrol., 388, 464–479, 2010.

Boon, S.: Snow ablation energy balance in a dead forest stand, Hydrol. Process., 23, 2600–2610, 2009.

10 Bréda, N. J.: Ground-based measurements of leaf area index: a review of methods, instruments and current controversies, J. Exp. Bot., 54, 2403–2417, 2003.

Chen, J. M., Rich, P. M., Gower, S. T., Norman, J. M., and Plummer, S.: Leaf area index of boreal forests: theory, techniques, and measurements, J. Geophys. Res., 102, 29429–29443, 1997.

Côté, J.-F., Widlowski, J.-L., Fournier, R., and Verstraete, M. M.: The structural and radiative 15 consistency of three-dimensional tree reconstructions from terrestrial lidar, Remote Sens. Environ., 113, 1067–1081, 2009.

Coops, N. C., Smith, M. L., Jacobsen, K. L., Martin, M., and Ollinger, S.: Estimation of plant and leaf area index using three techniques in a mature native eucalypt canopy, Austral. Ecol., 29, 332–341, 2004.

20 Coops, N. C., Varhola, A., Bater, C. W., Teti, P., and Boon, S.: Assessing differences in tree and stand structure following beetle infestation using LiDAR data, Can. J. Remote Sens., 35, 497–508, 2009.

Danson, F. M., Hetherington, D., Morsdorf, F., Koetz, B., and Allgöwer, B.: Forest canopy gap fraction from terrestrial laser scanning, IEEE Geosci. Remote S., 4, 157–160, 2007.

25 Ellis, C. R., Pomeroy, J. W., Brown, T., and MacDonald, J.: Simulation of snow accumulation and melt in needleleaf forest environments, Hydrol. Earth Syst. Sci., 14, 925–940, doi:10.5194/hess-14-925-2010, 2010.

Essery, R., Bunting, P., Hardy, J. P., Link, T., Marks, D., Melloh, R., Pomeroy, J. W., Rowlands, A., and Rutter, N.: Radiative transfer modeling of a coniferous canopy characterized by airborne 30 remote sensing, J. Hydrometeorol., 9, 228–242, 2007.

Field, A.: Discovering Statistics using SPSS, Sage Publications, 779 pp., 2005.

Discussion Paper | Discussion Paper | Discussion Paper | Discussion Paper |

Title Page

Abstract | Introduction

Conclusions | References

Tables | Figures

◄ | ►|

◄ | ►

Back | Close

Full Screen / Esc

Printer-friendly Version

Interactive Discussion

Frazer, G. W., Canham, C. D., and Lertzman, K. P.: Gap Light Analyzer (GLA), Version 2.0: Imaging software to extract canopy structure and gap light transmission indices from true-colour fisheye photographs, users manual and program documentation, Simon Fraser University/Institute of Ecosystem Studies, Burnaby, BC/Millbrook, NY, 1999.

5 Frazer, G. W., Fournier, R. A., Trofymow, J. A., and Hall, R. J.: A comparison of digital and film fisheye photography for analysis of forest canopy structure and gap light transmission, Agr. Forest Meteorol., 109, 249–263, 2001.

Goodwin, N., Coops, N. C., and Culvenor, D. S.: Assessment of forest structure with airborne LiDAR and the effects of platform altitude, Remote Sens. Environ., 103, 140–152, 2006.

10 Hanssen, K. H. and Solberg, S.: Assessment of defoliation during a pine sawfly outbreak: calibration of airborne laser scanning data with hemispherical photography, Forest Ecol. Manag., 250, 9–16, 2007.

Hardy, J. P., Melloh, R., Koenig, G., Marks, D., Winstral, A., Pomeroy, J. W., and Link, T.: Solar radiation transmission through conifer canopies, Agr. Forest Meteorol., 126, 257–270, 2004.

15 Hilker, T., van Leeuwen, M., Coops, N. C., Wulder, M. A., Newnham, G. J., Jupp, D. L. B., and Culvenor, D.: Comparing canopy metrics derived from terrestrial and airborne laser scanning in a Douglas-fir dominated forest stand, Trees, 24, 819–832, 2010.

Inoue, A., Yamamoto, K., Mizoue, N., and Kawahara, Y.: Calibrating view angle and lens distortion of the Nikon fish-eye converter FC-E8, J. Forest Res., 9, 177–181, 2004.

20 Jensen, J. L. R., Humes, K. S., Vierling, L. A., and Hudak, A. T.: Discrete return lidar-based prediction of leaf area index in two conifer forests, Remote Sens. Environ., 112, 3947–3957, 2008.

Jensen, J. L. R., Humes, K. S., Hudak, A. T., Vierling, L. A., and Delmelle, E.: Evaluation of the MODIS LAI product using independent lidar-derived LAI: a case study in mixed conifer 25 forest, Remote Sens. Environ., 115, 3625–3639, 2011.

Korhonen, L., Korpela, I., Heiskanen, J., and Maltamo, M.: Airborne discrete-return LIDAR data in the estimation of vertical canopy cover, angular canopy closure and leaf area index, Remote Sens. Environ., 115, 1065–1080, 2011.

Kraus, K. and Pfeifer, N.: Determination of terrain models in wooded areas with airborne laser 30 scanner data, ISPRS J. Photogramm. Remote Sens., 53, 193–203, 1998.

Kutner, M. C., Nachtsheim, C. J., Neter, J., and Li, W.: Applied linear statistical models, McGraw Hill, 1424 pp., 2005.

Title Page

Abstract | Introduction

Conclusions | References

Tables | Figures

◄ | ►|

◄ | ►

Back | Close

Full Screen / Esc

Printer-friendly Version

Interactive Discussion

Kuraś, P. K., Alila, Y., and Weiler, M.: Forest harvesting effects on the magnitude and frequency of peak flows can increase with return period, Water Resour. Res., 48, W01544, doi:10.1029/2011WR010705, 2012.

Leach, J. A. and Moore, R. D.: Above-stream microclimate and stream surface energy exchanges in a wildfire-disturbed riparian zone, Hydrol. Process., 24, 2369–2381, 2010.

Lee, H., Slatton, K. C., Roth, B. E., and Cropper, W. P.: Prediction of forest canopy light interception using three-dimensional airborne LiDAR data, Int. J. Remote Sens., 30, 189–207, 2009.

Lim, K., Treitz, P., Wulder, M., St.-Onge, B., and Flood, M.: LiDAR remote sensing of forest structure, Prog. Phys. Geog., 27, 88–106, 2003.

Lovell, J. L., Jupp, D. L., Culvenor, D. S., and Coops, N. C.: Using airborne and ground-based ranging lidar to measure canopy structure in Australian forests, Can. J. Remote Sens., 29, 607–622, 2003.

McGaughey, R. J.: FUSION/LDV: software for LIDAR data analysis and visualization, USDA Forest Service, 115 pp., 2010.

Morsdorf, F., Kötz, B., Meier, E., Itten, K., and Allgöwer, B.: Estimation of LAI and fractional cover from small footprint airborne laser scanning data based on gap fraction, Remote Sens. Environ., 104, 50–61, 2006.

Myers, R.: Classical and modern regression with applications. Duxbury, 486 pp., 1990.

Næsset, E.: Predicting forest stand characteristics with airborne scanning laser using a practical two-stage procedure and field data, Remote Sens. Environ., 80, 88–99, 2002.

Parviainen, J. and Pomeroy, J. W.: Multiple-scale modeling of forest snow sublimation: initial findings, Hydrol. Process., 14, 2669–2681, 2000.

Pomeroy, J. W. and Dion, K.: Winter radiation extinction and reflection in a boreal pine canopy: measurements and modelling, Hydrol. Process., 10, 1591–1608, 1996.

Pomeroy, J. W., Gray, D., Brown, T., Hedstrom, N., Quinton, W., Granger, R., and Carey, S.: The cold regions hydrological model: a platform for basing process representation and model structure on physical evidence, Hydrol. Process., 21, 2650–2667, 2007.

Riaño, D., Valladares, F., Condés, S., and Chuvieco, E.: Estimation of leaf area index and covered ground from airborne laser scanner (Lidar) in two contrasting forests, Agr. Forest Meteorol., 124, 269–275, 2004.

Rich, P. M., Wood, J., Vieglais, D. A., Burek, K., and Webb, N.: Hemiview User Manual. Delta-T Devices Ltd., Burwell, Cambridge, UK, 1999.

LiDAR canopy metrics relevant to hydrological modeling

A. Varhola et al.

Title Page

Abstract	Introduction
Conclusions	References
Tables	Figures

|◄ | ►|
◄ | ►

Back | Close

Full Screen / Esc

Printer-friendly Version

Interactive Discussion

Roberts, S. D., Dean, T. J., Evans, D. L., McCombs, J. W., Harrington, R. L., and Glass, P. A.: Estimating individual tree leaf area in loblolly pine plantations using LiDAR-derived measurements of height and crown dimensions, Forest Ecol. Manag., 213, 54–70, 2005.

Sicart, J. E., Essery, R., Pomeroy, J. W., Hardy, J. P., Link, T. E., and Marks, D.: A sensitivity study of daytime net radiation during snowmelt to forest canopy and atmospheric conditions, J. Hydrometeorol., 5, 774–784, 2004.

Solberg, S.: Mapping gap fraction, LAI and defoliation using various ALS penetration variables, Int. J. Remote Sens., 31, 1227–1244, 2010.

Solberg, S., Næsset, E., Hanssen, K. H., and Christiansen, E.: Mapping defoliation during a severe insect attack on Scots pine using airborne laser scanning, Remote Sens. Environ., 102, 364–376, 2006.

Solberg, S., Brunner, A., Hanssen, K. H., Lange, H., Næsset, E., Rautiainen, M., and Stenberg, P.: Mapping LAI in a Norway spruce forest using airborne laser scanning, Remote Sens. Environ., 113, 2317–2327, 2009.

Stenberg, P., Linder, S., Smolander, H., and Flower-Ellis, J.: Performance of the LAI-2000 plant canopy analyzer in estimating leaf area index of some Scots pine stands, Tree Physiol., 14, 981–995, 1994.

Teti, P.: Relations between peak snow accumulation and canopy density, Forest. Chron., 79, 307–312, 2003.

Teti, P.: Effects of overstory mortality on snow accumulation and ablation, Canadian Forest Service, Victoria, BC, 2008.

Teti, P.: Effects of overstory mortality on snow accumulation and ablation – Phase 2, Canadian Forest Service, Victoria, BC, 2009.

Todd, K. W., Csillag, F., and Atkinson, P. M.: Three-dimensional mapping of light transmittance and foliage distribution using lidar, Can. J. Remote Sens., 29, 544–555, 2003.

Uunila, L., Guy, B., and Pike, R.: Hydrologic effects of mountain pine beetle in the interior pine forests of British Columbia: key questions and current knowledge, Stream. Water. Manage. Bull., 9, 1–6, 2006.

Varhola, A., Coops, N. C., Weiler, M., and Moore, R. D.: Forest canopy effects on snow accumulation and ablation: an integrative review of empirical results, J. Hydrol., 392, 219–233, 2010a.

Title Page

Abstract | Introduction

Conclusions | References

Tables | Figures

◄ | ►

◄ | ►

Back | Close

Full Screen / Esc

Printer-friendly Version

Interactive Discussion

Varhola, A., Coops, N. C., Bater, C. W., Teti, P., Boon, S., and Weiler, M.: The influence of ground- and lidar-derived forest structure metrics on snow accumulation and ablation in disturbed forests, Can. J. Forest Res., 40, 812–821, 2010b.

Welles, J. M. and Cohen, S.: Canopy structure measurement by gap fraction analysis using commercial instrumentation, J. Exp. Bot., 47, 1335–1342, 1996.

Welles, J. M. and Norman, J. M.: Instrument for indirect measurement of canopy architecture, Agron. J., 83, 818–825, 1991.

Wigmosta, M., Vail, L., and Lettenmaier, D. P.: A distributed hydrology-vegetation model for complex terrain, Water Resour. Res., 30, 1665–1679, 1994.

Wigmosta, M., Nijssen, B., Storck, P., and Lettenmaier, D. P.: The distributed hydrology soil vegetation model. Mathematical models of small watershed hydrology and applications, edited by: Singh, V. and Frevert, D. K., Water Resource Publications, 7–42, 2002.

Wulder, M., Bater, C. W., Coops, N. C., Hilker, T., and White, J.: The role of LiDAR in sustainable forest management, Forest. Chron., 84, 807–826, 2008.

Zhao, K. and Popescu, S.: Lidar-based mapping of leaf area index and its use for validating GLOBCARBON satellite LAI product in a temperate forest of the southern USA, Remote Sens. Environ., 113, 1628–1645, 2009.

LiDAR canopy metrics relevant to hydrological modeling

A. Varhola et al.

Table 1. Stand locations and physical characteristics as of 2008.

Plot codes[a]	General information Stand description (age)	Latitude (°)	Longitude (°)	Elevation (m)	Ground inventory metrics Stem density (n ha^{-1})	DBH (cm)	Basal area (m^2 ha^{-1})	Mean height (m)	Max. height (m)	Foliage appearance (%)[b] Green	Red	Grey
BOD1	Mature heavily defoliated stand (216)	52.676	−123.016	1218	1800	18.5	55.4	18.2	28.9	0	19	77
BOD3	Mature defoliated stand (211)	52.638	−122.993	1222	550	25.5	28.7	17.3	26.2	8	14	77
BRC1	Small healthy regeneration (10)	52.670	−123.017	1231	1312	5.4	1.1	3.9	5.6	100	0	0
BRC2	Medium red-attack stand (26)	52.672	−123.017	1229	1025	13.5	15.0	10.1	13.5	48	52	0
VOD1	Mature defoliated stand (135)	53.720	−124.949	902	1387	18.0	19.0	9.0	17.3	22	0	78
VOD2	Mature heavily defoliated stand (135)	53.717	−124.955	836	1687	21.6	55.6	13.2	20.8	5	5	90
VYN	Dense natural post-fire stand (75)	53.719	−124.953	900	7648	8.0	34.0	9.7	14.3	75	0	25

[a] Following codes by Teti (2008); first letter in code corresponds to the study area.
[b] Defoliation percentage calculated as proportion of basal area falling into each health category, which are described by Varhola et al. (2010b).

Table 2. ALS simple metric summary for each major plot.

Plot codes	Stand description (age)	Total ALS returns	Ground ALS returns	Canopy ALS returns	Point density (n m^{-2})	Mean absolute scan angle (°)[a]	Vertical gap fraction	Maximum hit height (m)	Mean canopy return height (m)[a]
BOD1	Mature heavily defoliated stand (216)	13 521	10 042	3479	5.4	0.6 (118)	0.74	25.7	12.7 (55)
BOD3	Mature defoliated stand (211)	21 209	16 070	5139	8.5	7.7 (49)	0.76	23.8	12.3 (51)
BRC1	Small healthy regeneration (10)	18 273	15 275	2998	7.3	5.0 (32)	0.84	4.2	1.3 (52)
BRC2	Medium red-attack stand (26)	19 232	10 393	8839	7.7	4.2 (48)	0.54	11.6	5.5 (53)
VOD1	Mature defoliated stand (135)	17 095	12 899	4196	6.8	13.7 (9)	0.75	20.5	7.0 (68)
VOD2	Mature heavily defoliated stand (135)	17 014	13 611	3403	6.8	3.9 (46)	0.80	20.4	11.9 (42)
VYN	Dense natural post-fire stand (75)	19 699	9279	10 420	7.9	6.1 (27)	0.47	12.8	6.0 (46)

[a] Coefficients of variation (%) from individual returns in parentheses.

Title Page

Abstract | Introduction

Conclusions | References

Tables | Figures

◄◄ | ►►

◄ | ►

Back | Close

Full Screen / Esc

Printer-friendly Version

Interactive Discussion

Table 3. Hemispherical photo parameter calibration.

Parameter	Definition[a]/source of information	Baker Creek	Vanderhoof
Latitude (°)	Average of study area plots	52.664° N	53.719° N
Longitude (°)	Average of study area plots	123.011° W	124.952° W
Elevation (m)	Average of study area plots	1230	903
Slope/aspect (°)	Average of study area plots	0/0	0/0
Solar time step (min)	Time interval for which the sun's position is measured between sunrise and sunset for the full length of the growing season. GLA default value used.	5	5
Growing season start/end	These dates affect the range in the solar declination for the period of interest. In this case, the growing season was approximated to the winter period due to our later interest in snow processes.	1 Oct/31 May	1 Oct/31 May
Azimuth/zenith sky regions	Discrete areas of the sky hemisphere separated by equal-interval divisions of azimuth and zenith.	16/18	16/18
Data source	Method for deriving growing season above-canopy solar radiation data.	Modelled	Modelled
Solar constant (W m^{-2})	Total radiant flux of the sun on a perpendicular surface located outside the Earth's atmosphere at a mean distance of one astronomical unit. GLA default value used.	1367	1367
Cloudiness index	Site-specific measurement of cloudiness: fraction of extraterrestrial radiation that reaches the ground surface as total solar radiation. Values for both sites calculated as an average fraction of daily GLA-modelled extraterrestrial radiation and radiation measured in a weather station located in the Baker Creek area (Bewley et al., 2010).	0.49	0.49
Spectral fraction	Fraction of global solar radiation (0.25 to 25.0 µm) incident on a horizontal surface at the ground that falls within a limited range of the electromagnetic spectrum. Values set to 1.0 to include the entire spectrum.	1.0	1.0
Units	Units of measure used to compute the incident radiant flux density data output.	MJ m^{-2} d^{-1}	MJ m^{-2} d^{-1}
Beam fraction	Ratio of direct to total spectral radiation incident on a horizontal surface at the ground over a specified period, which is a function of cloud cover for supra-daily periods. Values calculated from cloudiness index as explained by Frazer et al. (1999).	0.44	0.44
Sky region brightness	Method for describing the intensity of the solar disk and diffuse sky. The selected Standard Overcast Sky (SOC) assumes that the zenith is three times as bright as the horizon.	SOC	SOC
Clear sky transmission coefficient	Factor that describes the regional clarity of the atmosphere with respect to the instantaneous transmission of direct (beam) radiation. Value used recommended for the area by Frazer et al. (1999).	0.6	0.6

[a] All definitions taken from Frazer et al. (1999).

LiDAR canopy metrics relevant to hydrological modeling

A. Varhola et al.

Table 4. Variable acronyms and description.

Variable	Units	Code	Definition[a]	GLA output column #	Modeling role	Source
Optical HP gap fraction	–	FGF_θ	Fraction between # of sky and total # of pixels summed for angles $\leq \theta$	10/6	Dependent (Y_S or Y_M)	Optical HP processed with GLA
Optical HP total radiation transmittance	$MJ\,m^{-2}\,d^{-1}$	FRT_θ	Absolute amount of total (direct + diffuse) below-canopy radiation summed for angles $\leq \theta$	32		
Optical HP sky-view factor	%	$FSVF_\theta$	Percentage of total sky area found in canopy gaps summed for angles $\leq \theta$	20		
Optical HP leaf area index	$m^2\,m^{-2}$	$FLAI_\theta$	Half of total effective leaf area per unit ground area integrated for angles $\leq \theta$	From appended output[b]		
ALS gap fraction	–	LGF_θ	Same as FGF_θ	10/6	Main independent (X_1)	Synthetic ALS hemispherical images processed with GLA
ALS total radiation transmittance	$MJ\,m^{-2}\,d^{-1}$	LRT_θ	Same as FRT_θ	32		
ALS sky-view factor	%	$LSVF_\theta$	Same as $FSVF_\theta$	20		
ALS leaf area index	$m^2\,m^{-2}$	$LLAI_\theta$	Same as $FLAI_\theta$	From appended output[b]		
ALS vertical gap fraction	–	LVGF	Ratio of ground/total ALS hits	–	Supporting independent (X_2, X_3, X_4, X_5)	ALS raw data in cylinders with radius matching θ
ALS canopy hit mean height	m	LMH	Mean ALS hit height above ground	–		
ALS hit density	$n\,m^{-2}$	LD	ALS hit spatial density (including ground hits)	–		
ALS mean scan angle	°	LSA	Mean absolute ALS scan angle	–		

[a] All definitions of GLA-derived variables have been taken from Frazer et al. (1999), where they are described with more detail.
[b] $FLAI_\theta$ and $LLAI_\theta$ are obtained from the appended output of GLA, where LAI 4 ring corresponds to $\theta = 60°$ and LAI 5 ring corresponds to $\theta = 75°$. For additional information on LAI see Welles and Norman (1991) and Stenberg et al. (1994).

Title Page

Abstract | Introduction

Conclusions | References

Tables | Figures

Back | Close

Full Screen / Esc

Printer-friendly Version

Interactive Discussion

Table 5. Correlation matrix showing the coefficient of correlation (r) between variables used in multiple regression (gap fraction only, for simplicity); non-significant ($p > 0.05$) values shown in bold.

Zenith AOV (θ)	Variable	FGF_θ	LGF_θ	LVGF	LMH	LD	LSA
30	FGF_θ	–					
	LGF_θ	0.75	–				
	LVGF	0.56	0.42	–			
	LMH	−0.41	−0.72	**0.10**	–		
	LD	−0.37	−0.46	−0.57	0.30	–	
	LSA	**0.11**	**0.01**	**−0.02**	0.17	**0.51**	–
45	FGF_θ	–					
	LGF_θ	0.85	–				
	LVGF	0.65	0.45	–			
	LMH	−0.50	−0.77	**0.09**	–		
	LD	−0.20	−0.25	−0.38	**0.03**	–	
	LSA	0.21	**0.11**	0.13	**0.05**	0.45	–
60	FGF_θ	–					
	LGF_θ	0.89	–				
	LVGF	0.64	0.48	–			
	LMH	−0.55	−0.77	**0.10**	–		
	LD	**0.03**	**−0.06**	−0.27	−0.22	–	
	LSA	0.24	0.15	0.24	0.01	0.42	–
75	FGF_θ	–					
	LGF_θ	0.92	–				
	LVGF	0.62	0.47	–			
	LMH	−0.56	−0.75	0.18	–		
	LD	**0.07**	**0.00**	−0.30	−0.32	–	
	LSA	0.20	0.13	0.34	0.07	0.17	–
90	FGF_θ	–					
	LGF_θ	0.93	–				
	LVGF	0.63	0.50	–			
	LMH	−0.56	−0.73	0.18	–		
	LD	**0.08**	**0.01**	−0.30	−0.32	–	
	LSA	0.20	0.13	0.34	**0.07**	0.17	–

Table 6. Multiple linear regression results (refer to Table 4 for RMSE and $RMSE_S$ units).

Model variables[a]	Zenith cut (θ)	Adjusted R^2	RMSE	$RMSE_S$	$RMSE_N$	β_0	β_1	β_2	β_4	p Anderson-Darling	p Shapiro-Wilk
FGF_θ/	30	0.64	0.10	0.10	0.13	-0.15^b	0.71^c	0.39^c	0.01^b	0.00	0.00
LGF_θ	45	0.82	0.07	0.07	0.10	-0.24^c	0.68^c	0.44^c	0.00^c	0.37	0.29
	60	0.88	0.06	0.06	0.08	-0.34^c	0.63^c	0.42^c	0.03^c	0.16	0.17
	75	0.91	0.05	0.05	0.07	-0.38^c	0.57^c	0.41^c	0.03^c	0.58	0.89
	90	0.92	0.03	0.04	0.06	-0.26^c	0.52^c	0.28^c	0.02^c	0.53	0.74
$FSVF_\theta$/	30	0.64	1.28	1.28	0.13	-2.02^b	0.71^c	5.18^c	0.13^b	0.00	0.00
$LSVF_\theta$	45	0.82	2.00	2.03	0.10	-7.07^c	0.68^c	12.77^c	0.39^c	0.40	0.28
	60	0.88	2.83	2.86	0.08	-17.2^c	0.64^c	21.37^c	1.36^c	0.15	0.19
	75	0.91	3.54	3.58	0.07	-28.26^c	0.58^c	30.99^c	2.40^c	0.61	0.79
	90	0.92	3.67	3.71	0.06	-27.32^c	0.53^c	30.52^c	2.45^c	0.60	0.71
FRT_θ/	30	0.65	0.15	0.15	0.13	-0.25^b	0.73^c	0.59^c	0.02^b	0.00	0.00
LRT_θ	45	0.81	0.27	0.27	0.10	-0.82^c	0.68^c	1.60^c	0.05^c	0.51	0.67
	60	0.86	0.39	0.39	0.08	-1.92^c	0.62^c	2.56^c	0.17^c	0.69	0.96
	75	0.89	0.46	0.46	0.08	-3.02^c	0.57^c	3.55^c	0.27^c	0.08	0.07
	90	0.89	0.47	0.47	0.08	-3.13^c	0.55^c	3.66^c	0.29^c	0.10	0.07
$FLAI_\theta$/	60	0.76	0.25	0.25	0.10	2.32^c	0.61^c	-1.53^c	-0.09^c	0.06	0.00
$LLAI_\theta$	75	0.76	0.29	0.29	0.11	2.61^c	0.59^c	-1.76^c	0.11^c	0.01	0.00
$FLAI_\theta^{0.5}$/	60	0.80	0.12	0.12	0.08	1.63^c	0.33^c	-0.82^c	-0.04^c	0.36	0.01
$LLAI_\theta$	75	0.81	0.12	0.12	0.09	1.75^c	0.30^c	-0.82^c	-0.06^c	0.08	0.00

[a] Dependent (Y_M)/main independent (X_1) variables; supporting variables X_2 and X_4 are common for all models.
[b] Significant with $0.01 \leq p < 0.05$;
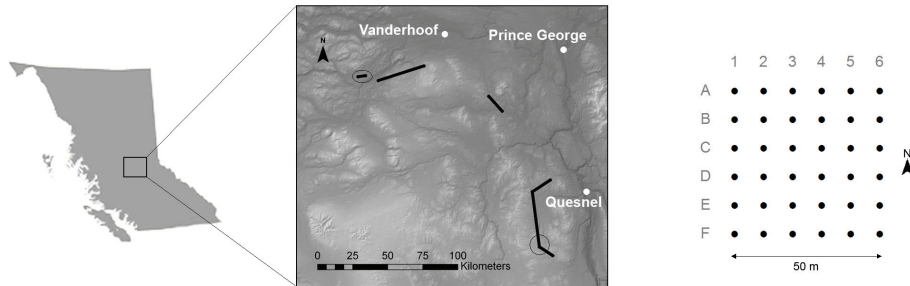[c] Significant with $p < 0.01$.

Fig. 1. Study area location within British Columbia (left) including ALS transects (black straight lines in the close-up) and ground plot locations in the Vanderhoof (top left corner ellipse) and Baker Creek (bottom right corner circle) areas; the 2500 m^2 square ground plots (right) are constituted by 36 individual stakes (spaced 10 m) labelled as letter and number combinations (A1 to F6) (Teti, 2008).
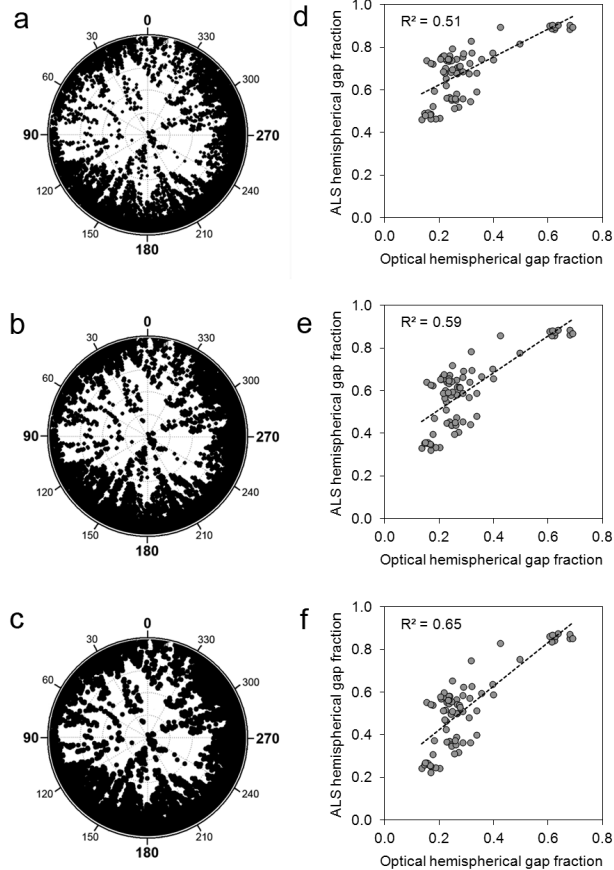
Fig. 2. Effect of projected ALS return size on the relationship between observed and predicted gap fractions. The projected circle size of synthetic image examples **(a–c)** and corresponding relationships **(d–f)** is expressed as the fraction between the diameter of each ALS return and the radius of the image: 0.0137 **(a, d)**, 0.0176 **(b, e)**, and 0.0215 **(c, f)**.
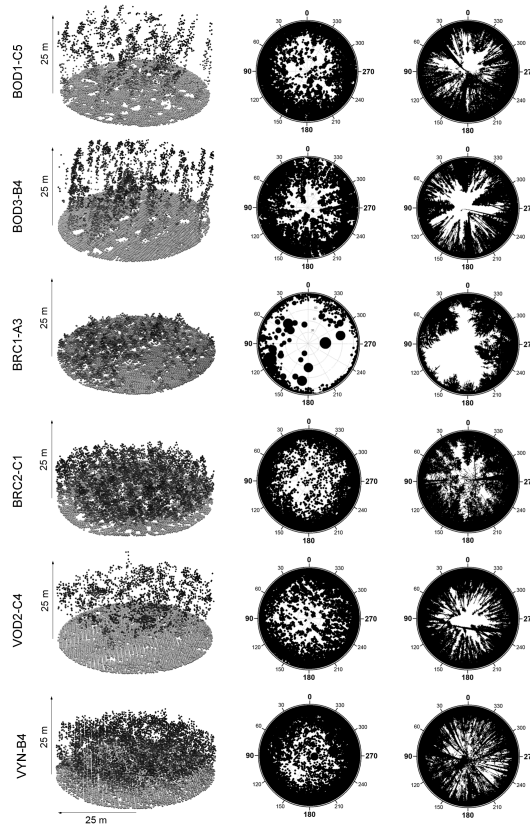
Fig. 3. Representative examples of ALS point clouds (left), ALS synthetic hemispherical images (center) and real optical hemispherical photographs (HP) (right) for each stand; azimuths (°) are shown on the hemispherical illustrations.

Title Page

Abstract | Introduction

Conclusions | References

Tables | Figures

|◄ | ►|

◄ | ►

Back | Close

Full Screen / Esc
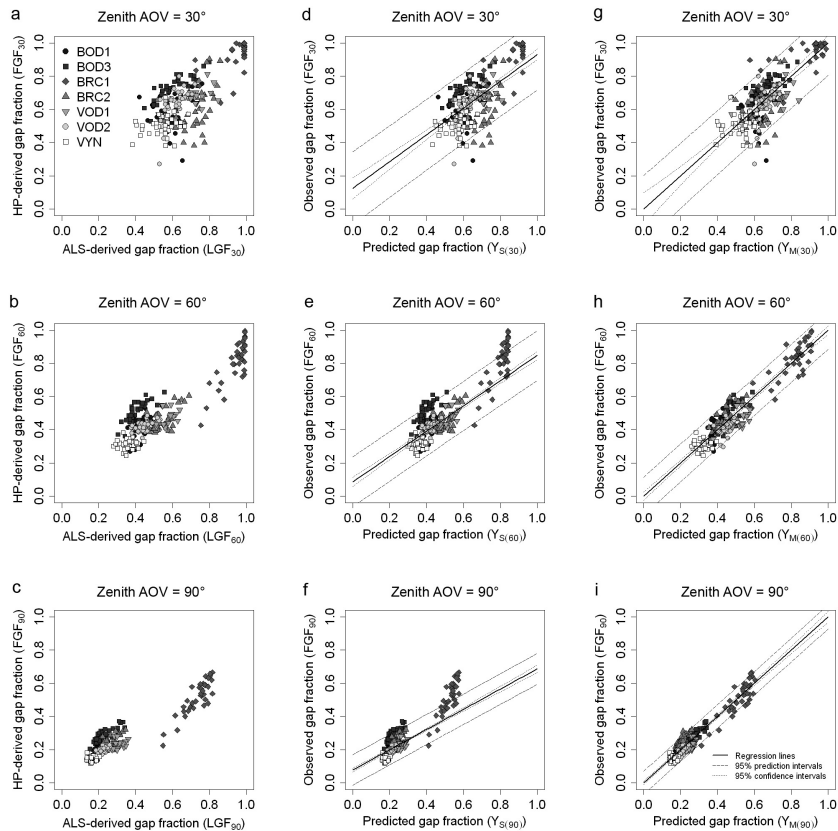
Printer-friendly Version

Interactive Discussion

Fig. 4. Relationship between ALS-derived (LGF_θ) and HP-derived gap fraction (FGF_θ) **(a–c)** and between predicted and observed values of gap fraction obtained from simple **(d–f)** and multiple **(g–i)** linear regression models across three representative zenith AOV (30°, top; 60°, center; and 90°, bottom); legends in sub-figures **(a)** and **(i)** apply to all.

Title Page

Abstract | Introduction

Conclusions | References

Tables | Figures

|◄ | ►|

◄ | ►

Back | Close

Full Screen / Esc

Printer-friendly Version

Interactive Discussion
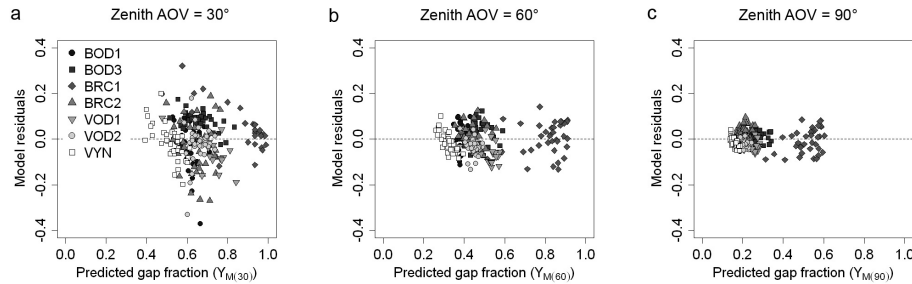
Fig. 5. Relationship between gap fraction predicted from multiple linear regression (Eq. 3) ($Y_{M(\theta)}$) and model residuals ($\mathrm{FGF}_{\theta} - Y_{M(\theta)}$) for three representative zenith AOV.

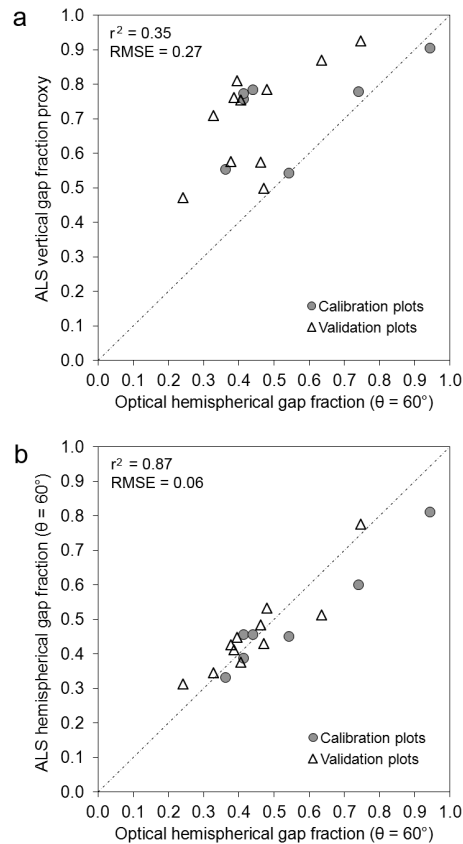**LiDAR canopy metrics relevant to hydrological modeling**

A. Varhola et al.

Fig. 6. Comparison between the relationship of plot-level average gap fractions obtained from optical HP and **(a)** vertical gap fraction estimated from untransformed ALS, and **(b)** gap fractions from calibrated synthetic hemispherical images.